



**HAL**  
open science

## Detection of Individual Conducting Graphene Nanoplatelet by Electro-catalytic Depression

Zejun Deng, Fouad Maroun, Jeffrey E Dick, Christophe Renault

► **To cite this version:**

Zejun Deng, Fouad Maroun, Jeffrey E Dick, Christophe Renault. Detection of Individual Conducting Graphene Nanoplatelet by Electro-catalytic Depression. *Electrochimica Acta*, 2020. hal-03018776

**HAL Id: hal-03018776**

**<https://hal.archives-ouvertes.fr/hal-03018776>**

Submitted on 23 Nov 2020

**HAL** is a multi-disciplinary open access archive for the deposit and dissemination of scientific research documents, whether they are published or not. The documents may come from teaching and research institutions in France or abroad, or from public or private research centers.

L'archive ouverte pluridisciplinaire **HAL**, est destinée au dépôt et à la diffusion de documents scientifiques de niveau recherche, publiés ou non, émanant des établissements d'enseignement et de recherche français ou étrangers, des laboratoires publics ou privés.

# Detection of Individual Conducting Graphene Nanoplatelet by Electro-catalytic Depression

Zejun Deng<sup>a</sup>, Fouad Maroun<sup>a</sup>, Jeffrey E. Dick<sup>b, c</sup>, Christophe Renault<sup>a, \*</sup>

<sup>a</sup>Laboratoire de Physique de la Matière Condensée, Ecole Polytechnique, CNRS, IP Paris, 91128 Palaiseau, France

<sup>b</sup>Department of Chemistry, The University of North Carolina at Chapel Hill, Chapel Hill, NC, 27599-3290, USA

<sup>c</sup>Lineberger Comprehensive Cancer Center, School of Medicine, The University of North Carolina at Chapel Hill, Chapel Hill, NC, 27599-3290, USA

\* Corresponding author, e-mail: [christophe.renault@polytechnique.edu](mailto:christophe.renault@polytechnique.edu)

**Abstract:** We report a strategy to electrochemically detect individual conducting particles colliding with an ultra-microelectrode (UME). This method, called “electro-catalytic depression” (ECD), enables the detection of particles that are electrically conducting but catalytically inert, such as carbonaceous particles. The ECD method takes advantage of the intrinsic difference in heterogeneous kinetics of electron transfer for a given inner-sphere reaction to block the current at the surface of a particle made of a material having poor catalytic properties compared to the material of the electrode. We showcase this method with the detection of individual graphene nanoplatelets (GNPs) of few  $\mu\text{m}$  long and 15 nm thick. GNPs block the oxidation of hydrazine on a 5  $\mu\text{m}$  radius Pt UME. We studied the influence of the potential on the current transient produced by individual GNP stochastically colliding on the UME. We evidence that, under 0.1 V vs AgAgCl 3.4 M KCl, electrically conducting GNPs produce discrete stair-shaped drops of current (negative steps) similar to the signal obtained with insulating particles like polystyrene beads. We show how the analysis of a “blocking-type” signal originally developed for insulating beads can be extended to the detection of conducting particles. However, at high potentials ( $> 0.1$  V), where hydrazine oxidation occurs on the GNP, the kinetic difference between GNP and Pt decreases, leading to the decrease of both average and median current step size and the appearance of positive steps. The frequency of collision versus the concentration of GNP and the bias potential are discussed.

**Keywords:** analytical electrochemistry, single entity electrochemistry, graphene nanoplatelets, hydrazine oxidation

## 1. Introduction

Stochastic collision enables the detection of a wide variety of individual entities such as metal nanoparticles [1, 2], emulsion droplets [3, 4], vesicle [5, 6], micelles [7], proteins [8] and bacteria [9]. Depending on the nature of the entity (insulator, conductor, redox-active material), various electrochemical detection schemes can be used [10]. Insulating objects can be detected by “electrochemical blocking”. This strategy, initially reported by Lemay and coworkers [11], relies on a “turn-off” type of response. A redox reporter is oxidized/reduced at a UME and a steady-state current is measured. Upon stochastic collision and subsequent irreversible adsorption of an individual insulating object, a portion of volume above the electrode is blocked and a discrete decrease of current (a “current step”) is observed. The magnitude of the current step can be linked to the size of the object provided that the radial position of the object on the electrode is known [12]. We recently showed that using hemispherical UMEs instead of disk UMEs enables the quantitative

1 determination of the size without knowing the radial position [13]. The frequency of collision can  
2 be used to determine the concentration or charge of the objects in solution [13, 14].

3 Conducting nanoparticles require a different strategy to produce an electrochemical signal.  
4 Bard and coworkers developed a method called electro-catalytic amplification to detect particles  
5 made of a material that possesses, for a given inner-sphere reaction, “good” catalytic properties  
6 compared to the material of the electrode [1, 2]. Thus, the electrode does not produce any faradaic  
7 current by itself while the reaction is switched on when an individual catalytic nanoparticle is in  
8 contact with the underlying electrode. Catalytic amplification is extremely sensitive since it is a  
9 “turn-on” type of detector and the analysis of the frequency of collision can lead to the concentra-  
10 tion of particle in solution. The analysis of the step size can, in principle, lead to the size of the  
11 particle. However, among eighteen examples of catalytic amplification [15, 16], only four cases  
12 show ideal step-like events [2, 17-19] while the others report spike-shaped current events. This  
13 peculiar shape is attributed to the deactivation of the particle and the shift of equilibrium potential  
14 during the collision [19, 20].

15 Redox-active objects such as silver nanoparticles or droplets and vesicles loaded with a redox  
16 molecule can be detected individually by electrolysis [3, 21-23]. Upon collision of a redox-active  
17 object on a UME, the redox content of the object is electrolyzed, generating a spike-shaped current  
18 event. The integration of each current event provides an amount of charge, directly related to the  
19 size of the object via Faraday’s law of electrolysis. This correlation is possible when the particles  
20 undergo full oxidation [24-27].

21 The detection of non-redox active materials that are neither insulators nor good catalysts like  
22 carbonaceous materials remains a challenge. Detection of carbonaceous particles by electrochemi-  
23 cal collision is reported for carbon nanotubes [28], graphene sheets [29], and graphene nanoplate-  
24 lets (GNP) [30]. The detection of single-wall carbon nanotubes relies on area amplification [28].  
25 The size of the nanotube should be larger than the size of the electrode. Upon collision of the carbon  
26 nanotube on a UME, a discrete increase of current can be evidenced by measuring the electrochemi-  
27 cal response of a redox couple in solution. Note that ideal discrete increases of current were ob-  
28 served only for carbon nanotubes modified with gold nanoparticles but not for bare carbon nano-  
29 tubes. The detection of a single graphene sheet was performed using a “tunneling” strategy consist-  
30 ing in adsorbing a conducting particle on an electrode passivated with an insulating layer thin  
31 enough to allow tunnelling [29]. Cyclic voltammetry on an individual graphene sheet enable the  
32 estimation of its size. The incubation of the electrode in the suspension of the graphene sheet was  
33 performed blindly (that is without monitoring the collisions) and thus the adsorption of individual  
34 graphene sheets was not observed in real-time and no analysis of the frequency of collision was  
35 performed. The third example relies on transient currents recorded upon collision of individual  
36 GNPs on a C-fiber UME [30]. Current transients were counted to estimate a concentration of GNP  
37 in solution. The authors proposed that current transients are generated by charging the capacitance  
38 of individual GNPs.

39 Here, we propose an alternative strategy, electro-catalytic depression (ECD), to detect carbo-  
40 naceous particles. We study GNPs. These particles are used for a wide range of applications: dye-  
41 sensitized solar cells [31, 32], conducting support for loading catalysts [33, 34], supercapacitors  
42 [35], and sensors [36]. In this article, commercial GNPs with few microns in width and about 15  
43 nm in thickness are used. We take advantage of the intrinsic difference in electron transfer kinetics  
44 for an inner-sphere reaction, hydrazine oxidation, to drive a current through a UME made of a good

1 catalyst (Pt), while kinetically blocking the current at the surface of a GNP. The frequency of col-  
2 lision versus the concentration of GNP and the potential is investigated. Also, we discuss the effect  
3 of the interplay between the distribution of the current step size, the kinetic difference between Pt  
4 and GNP and the potential.

## 5 **2. Experimental Section**

### 6 **2.1 Chemicals and Reagents.**

7 GNPs ( $\approx 5 \mu\text{m}$  particle size, 15 nm thickness, Sigma Aldrich), hydrazine monohydrate ( $\text{N}_2\text{H}_4$   
8 64-65%, > 98%, Sigma Aldrich), ferrocene methanol (97%, Sigma Aldrich) and sodium hydroxide  
9 (0.1 M NaOH solution, Fluka) were used without further purification. Solutions were prepared with  
10 deionized water (Millipore Milli-Q,  $18.2 \text{ M}\Omega \cdot \text{cm}^{-1}$ ).

### 11 **2.2 Fabrication of Pt and C-fiber UMEs.**

12 The  $5 \mu\text{m}$  radius disk Pt UMEs are fabricated by heat-sealing a  $5 \mu\text{m}$  radius Pt wire (hard  
13 tempered, Goodfellow) inside a borosilicate glass capillary (outer diameter: 2 mm, inner diameter:  
14 1.16 mm, Sutter Instrument). A tungsten wire ( $250 \mu\text{m}$  diameter, Goodfellow) was glued on the Pt  
15 wire using conducting silver epoxy (Araldite). More details about the fabrication and polishing  
16 procedures can be found in the following reference [13]. C-fiber UMEs are fabricated by first gluing  
17 a c.a. 1 cm long  $3.5 \mu\text{m}$  radius C-fiber (XAS quality, Goodfellow) on a tungsten wire with conduct-  
18 ing Ag epoxy and then, casting the fiber and a portion of the tungsten wire into a hard epoxy  
19 (EpoHeat, Buehler) contained within a plastic pipette cone. The C-fiber UME is polished following  
20 the same procedure as the Pt UME.

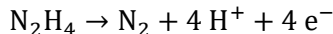
### 21 **2.3 Electrochemical measurements.**

22 All electrochemical measurements were performed using a homemade two-electrode setup  
23 placed in a Faraday cage. Briefly, a USB-6212 acquisition card (National Instruments) is used to  
24 apply a potential at the working electrode and measure the current after its amplification with a  
25 trans-impedance current amplifier (DPPCA-300, Femto GmbH). The amplifier has a gain of  $10^9$   
26 V/A with a bandwidth of 150 Hz. Points are acquired every 6.7 ms and averaged to obtain a current  
27 value every 50 ms. Detailed information about the setup is provided in the following reference [13].  
28 Chronoamperograms are recorded for 120 s or 900 s for each collision experiment. Before each  
29 collision experiment, chronoamperograms are recorded for 120 s in the absence of GNPs to ensure  
30 that no steps are observed (i.e., negative control). A 35 fM GNP suspension was prepared by adding  
31 2 mg of GNPs to 200 ml of  $10 \mu\text{M}$  NaOH electrolyte solution, assuming that GNP has a regular  
32 circular shape with a radius of  $2.1 \mu\text{m}$  obtained from SEM (vide infra). Between experiments, the  
33 Pt UME is polished and then cleaned by dipping few tens of seconds in a Piranha solution (3:1 v of  
34 98% sulfuric acid and 30%  $\text{H}_2\text{O}_2$ ) to remove the GNPs. A leakless miniature Ag/AgCl 3.4 M KCl  
35 electrode (ET072 from eDAQ) is used as both the reference and counter electrode. All potentials  
36 will be quoted against this reference electrode. The solutions are degassed by bubbling Ar for few  
37 minutes prior to the measurements.

## 38 **3. Results and Discussion**

### 39 **3.1 Kinetics of hydrazine oxidation on Pt UME vs. C-fiber UME**

40 Hydrazine oxidation is a four-electron reaction:



The pKa of hydrazine is 8.1 [37]. In the presence of 10  $\mu\text{M}$  of NaOH in solution, hydrazine is deprotonated and the concentration of  $\text{N}_2\text{H}_5^+$  is negligible ( $\sim 30 \mu\text{M}$ ) compared to the bulk concentration of hydrazine (1mM). Figure 1A shows typical cyclic voltammograms of hydrazine oxidation on a 3.5  $\mu\text{m}$  radius C-fiber UME (black traces) and a 5  $\mu\text{m}$  radius Pt UME (red traces), along with the corresponding blanks (dashed lines) recorded in the absence of hydrazine. The blanks do not show any faradaic current except the beginning of water oxidation at ca. 1.5 V on the C-fiber UME. In the presence of hydrazine, the current starting at -0.6 V for the Pt UME and 0.1 V for the C-fiber UME is caused by hydrazine oxidation. The cyclic voltammogram recorded with the Pt UME displays two plateaus of current ( $i_{\text{ss}}^1 = 4.5 \text{ nA}$  and  $i_{\text{ss}}^2 = 10.8 \text{ nA}$ ). The plateau of current corresponding to the theoretical diffusion-limited current on a disk UME is given by equation 1 [38]:

$$i_{\text{ss}} = 4nFD_{\text{redox}}C_{\text{redox}}r_{\text{elec}} \quad (1)$$

where  $n$  is the number of electrons exchanged per molecule,  $F$  is the Faraday's constant,  $D_{\text{redox}}$  is the diffusion coefficient of the redox molecule,  $C_{\text{redox}}$  is the bulk concentration of the redox molecule, and  $r_{\text{elec}}$  is the radius of the electrode. Using our experimental parameters ( $r_{\text{elec}} = 5.0 \mu\text{m}$ ,  $n = 4$ ,  $C_{\text{redox}} = 1 \text{ mM}$  and  $D_{\text{redox}} = 1.4 \times 10^{-5} \text{ cm}^2 \cdot \text{s}^{-1}$ ) a theoretical limiting current of  $i_{\text{ss}} = 10.8 \text{ nA}$  is calculated [39, 40]. Thus, the second plateau at c.a. 10.8 nA on the red cyclic voltammogram in Figure 1A is attributed to the diffusion-limited current for hydrazine oxidation. The inflection point of the first and second sigmoids are around -0.4 V and 0.2 V, respectively. These values are close to the apparent standard potential reported for hydrazine oxidation in basic ( $\text{pH} \approx 8$ ) and acidic ( $\text{pH} \approx 1-2$ ) conditions, respectively [41, 42]. The first plateau (c.a. 4.5 nA) on the cyclic voltammogram of the Pt UME is attributed to a local change of pH at the surface of the electrode when hydrazine is oxidized. Indeed, the products of hydrazine oxidation are nitrogen and protons that will locally acidify the solution causing a shift of the apparent standard potential [43]. We verified this point by fixing the pH with increasing concentrations of NaOH and observing the complete disappearance of the intermediate plateau when the concentration of NaOH is about five times larger than the concentration of hydrazine (Figure S1 in SI). The cyclic voltammogram recorded with the C-fiber UME displays one plateau ( $i_{\text{ss}} \approx 3.8 \text{ nA}$ ) followed by an increase of the current above 1.5 V. The oxidation of water above 1.5 V masks the second plateau of hydrazine oxidation that should also be observed with the C-fiber UME.

Importantly, the oxidation of hydrazine on a C-fiber UME is extremely sluggish, as shown by the width (ca. 1 V) of the sigmoid (black trace in Figure 1A) and the onset potential 700 mV more positive on the Pt UME than the C-fiber UME. It is thus possible to find a potential window where the current of hydrazine oxidation is large on Pt while it remains extremely small on carbon. For example, at 0 V (blue arrow on Figure 1A) the current is hundreds of times larger on the C-fiber UME than on the Pt UME. At such potential, carbonaceous particles possessing kinetics of hydrazine oxidation similar to that of C-fiber can be considered as an inert surface and are expected to block the current when colliding on a Pt UME. In the following, we will assume that the overall shape of the CV of a GNP is similar to that of C-fiber presented in Figure 1A (solid black line) but with slower kinetics. This assumption is verified with collision experiments of GNP performed on a C-fiber UME (Figure S2 in SI). This assumption is also based on the potential dependent current step sizes of GNP on Pt that we observed (shown later in this paper).

The size and morphology of the GNPs were characterized by SEM (see inset in Figure 1B and Figure S3 in SI). The morphology of the GNP is relatively ill-defined, and thus we quantified their

1 size by averaging the longest and shortest axis of the platelets. Their size distribution is plotted in  
2 the histogram Figure 1B. The average length is about  $4.2 \pm 2.5 \mu\text{m}$ . The GNPs can be suspended at  
3 35 fM to 70 fM in water in the presence of  $10 \mu\text{M}$  NaOH. The presence of a base helps stabilizing  
4 carbonaceous particles in water [44]. Concentrations of NaOH larger than  $10 \mu\text{M}$  or GNP concen-  
5 trations larger than  $140 \text{ fM}$  induce sedimentation within few minutes. Although this issue could  
6 have been addressed by adding surfactants in solution, these latter were not used because of their  
7 adverse effect on the oxidation of hydrazine at the Pt surface.

### 8 **3.2 Detection of individual GNPs by ECD**

9  
10 Figure 2A shows two typical chronoamperograms obtained with a  $5 \mu\text{m}$  radius Pt UME biased  
11 at 0 V in a 1 mM hydrazine and  $10 \mu\text{M}$  NaOH solution in the presence (red trace) and the absence  
12 (black trace) of 35 fM GNPs. In the absence of GNP, the oxidation of hydrazine on the Pt UME  
13 leads to a quasi-steady-state current (the black trace in

14 Figure 2B) of a few nA. Importantly, no abrupt change of current is observed. However, in  
15 the presence of GNPs, discrete stair-shaped current decays are observed on the red trace in

16 Figure 2A. A zoom on typical current steps is shown in

17 Figure 2B. Current steps were consistently observed in 19 individual experiments in the pres-  
18 ence of GNPs but never in the blanks (i.e., in the absence of GNP). The observation of discrete  
19 decreases of current confirms that GNPs are kinetically blocking hydrazine oxidation on the Pt  
20 UME at a potential of 0 V. To prove this point, we also performed experiments with an outer-sphere  
21 redox couple (ferroceniummethanol/ferrocenemethanol), displaying fast kinetics of electron trans-  
22 fer on both Pt and carbon electrodes. A typical chronoamperogram is shown in Figure S4 in SI. No  
23 negative current steps are observed when the kinetics of electron transfer is as fast on Pt as on GNP.

24 Figure 2C illustrates how this kinetic blocking takes place. Single GNPs collide on the Pt  
25 surface and partially cover this latter preventing locally the oxidation of hydrazine.

26 Apart from typical stair-shaped events (91% of all events), we also observe in rare occasions  
27 square-shaped events (5% of all events) as well as spike-shaped events (4% of all events). Examples  
28 of these events are shown in Supporting Information (Figure S5 in SI). The staircase-shaped events  
29 are attributed to GNPs irreversibly adsorbing on the Pt surface. The square-shaped events are at-  
30 tributed to GNPs that are first adsorbing on the Pt surface and then leaving in solution. These two  
31 kinds of events are also observed for “blocking” type experiments with polystyrene beads [13]. The  
32 spike-shaped events are possibly caused by GNPs bouncing on the UME surface and thus display-  
33 ing a short residence time ( $0.13 \pm 0.04 \text{ s}$  on average). Spike-shaped current events are also reported  
34 for gold nanoparticles bouncing at the surface of gold electrodes modified with self-assembled  
35 monolayers of alkanethiols [45]. In the following sections, we will focus on the “sticking” GNPs.

36 The ideal shape of the current events allows a precise measurement of  $\Delta i/i_{ini}$ . The histogram  
37 of the relative current step size is given in Figure S6 in SI. However, the quantitative analysis of  
38 the step-size is rendered difficult by the inhomogeneity of the shape and size of the GNPs as well  
39 as the edge effect always present on a disk-shaped electrode [12]. Numerical simulations of “ideal”  
40 GNPs having a disk shape and blocking the center and the edge of the UME were carried out.  
41 Details about the simulation can be found in Supporting Information. We found that GNPs between

1 0.5 and 3.5  $\mu\text{m}$  in diameter could produce the minimum and maximum relative current steps ob-  
2 served in the chronoamperograms. This range of size is significantly lower than the size distribution  
3 obtained by SEM (c.a. 0.6 – 20  $\mu\text{m}$ ). In order to understand this discrepancy, we monitored optically  
4 (using bright field microscopy) the solution containing the GNPs directly after dispersion. We  
5 found that GNPs between 4 and 20  $\mu\text{m}$  sediment within two minutes (time scale of our experiments)  
6 on the bottom of the cell (see Figure S9 in SI). Since our UME is facing downward, it is expected  
7 that the sedimentation of the large GNPs will hinder their collision.

### 8 **3.3 Collision frequency vs. concentration of GNP**

9 The average frequency of collision at 0 V is plotted as a function of the concentration of GNP  
10 in

11 Figure 3. The frequency of collision was calculated from 11 individual chronoamperometric  
12 experiments and we only counted the first six collisions to minimize a possible effect of GNP  
13 stacking on the electrode. Representative chronoamperograms for different concentrations of GNP  
14 in solution are given in Figure S10 in SI. The collision frequency is in the range of 0.2 Hz to 0.8  
15 Hz. It increases with the concentration of GNP and then seems to saturate at a concentration above  
16 140 fM. The deviation from linearity (expected for diffusion-drift mass transport) could be caused  
17 by the aggregation and subsequent sedimentation of the GNP. Such deviation is also reported for  
18 the collision frequency of Pt nanoparticles on Hg UMEs [46, 47]. In that case, collision frequencies  
19 lower than expected were also explained by the poor stability of the particles [47]. In a nutshell, the  
20 stability of the colloidal suspension is of crucial importance to accurately determine the concentra-  
21 tion.

22 The collision frequency is related to the origin of the GNP transport in the electrolyte. The  
23 arrival of the GNPs to the Pt surface cannot be ensured by diffusion because the estimated value of  
24 the collision frequency at 35 fM is of the order of 0.05 mHz at 0 V (see SI) which is lower by more  
25 than 3 orders of magnitude than the measured value (0.2 Hz). GNP migration should then play a  
26 major role. Indeed, GNPs are charged (the zeta-potential is  $\zeta\text{-V} = 32.5 \pm 0.3$  mV under our experi-  
27 mental conditions) and the ionic strength is kept extremely low ( $\sim 40$   $\mu\text{M}$ ). The expected value of  
28 the collision frequency induced by migration at 35 fM is 1.8 Hz (see SI). The theoretical frequency  
29 of collision is nine times higher than the experimental frequency of collision (0.2 Hz). As discussed  
30 previously, the suspension of GNP is unstable and thus the nominal concentration is larger than the  
31 concentration of GNP dispersed in solution. The collision frequency would be overestimated in  
32 proportion to the error on the concentration of GNP. Another factor to consider is the local ionic  
33 strength decreasing the contribution of migration to the collision frequency. Indeed, we evidenced  
34 a local decrease of the pH by several units of pH indicating an ionic strength significantly larger  
35 near the UME than in the bulk.

36 We also measured the average collision frequency (more than twenty individual measure-  
37 ments) at potentials of -0.3 V, 0 V, 0.7 V and 1.0 V. The corresponding steady-state currents /  
38 frequency of collision are c.a. 2 nA / 0.10 Hz, 4 nA / 0.20 Hz, 9 nA / 0.24 Hz and 11 nA / 0.24 Hz,  
39 respectively. We observe a clear increase of the collision frequency with potential, which seems to  
40 saturate at 0.7 V. In a migration dominated mass transport, the collision frequency is expected to  
41 increase proportionally with the current. The experimental trend significantly deviates from this  
42 linear dependence. In a similar way to what has been shown above, the saturation of the collision

1 frequency may be ascribed to the local increase of the ionic strength due to the release of protons  
2 during hydrazine oxidation.

### 3 3.4 Step size vs. potential

4 The histograms of the normalized size distribution of the relative current step (i.e., the current  
5 step,  $\Delta i$ , divided by the current right before the step,  $i_{ini}$ ) are plotted in

6 Figure 4 for four different potentials. Typical chronoamperograms at different potentials are  
7 given in SI (Figure S11 and Figure S12). About 200 negative steps (for each potential) were rec-  
8 orded to provide a statistically significant description of the magnitude of the current steps and  
9 investigate the effects of the potential. Each experiment corresponds to a freshly polished Pt UME.  
10 In order to avoid the formation of multilayers, only the first six collisions are counted, considering  
11 that an “ideal” GNP is a disk with a diameter of 4.2  $\mu\text{m}$  and has a surface area of 13.8  $\mu\text{m}^2$ , around  
12 six times smaller than the Pt surface (78.5  $\mu\text{m}^2$ ).

13 The trend observed in

14 Figure 4 is the shift of the current distribution to lower values with increasing potentials, as  
15 indicated by the green dash arrow. This shift is small at 0.7 V (blue symbols) but significant at 1 V  
16 (orange symbols). We calculated the average, median, and distribution range obtained for each  
17 histogram (Table 1). The average (and median) step size is constant between 0.3 V and 0 V and  
18 then decreases by 15% (respectively 24%) as the potential increases from 0 V to 0.7 V (respectively  
19 1 V).

20 **Table 1.** The statistical description of the magnitude of the negative steps at different bias potentials.

Potential (V)	Counts	Average (‰)	Median (‰)	*Range (‰)
-0.3	201	8.0	5.3	1 to 55
0	198	8.0	5.4	1.1 to 54
0.7	202	6.8	4.5	0.7 to 42
1.0	210	6.1	3.7	0.6 to 39

21 \* For 95% of the range (for all the potentials) the maximum step is about 21‰.

22 In order to understand the variation of the average step size, as a function of the potential we  
23 will examine the kinetics of hydrazine oxidation on Pt and carbon.

24 Figure 5A shows the adimensional voltammograms (forward scan only) corresponding to hy-  
25 drazine oxidation on Pt (black curve) and C-fiber (red curve), a proxy for the surface of the GNPs.  
26 The blue curve,  $\Delta i$ , represents the current difference between hydrazine oxidation on Pt and C-fiber.  
27 The trace corresponding to  $\Delta i$  overlaps with the voltammogram of the Pt UME from the onset  
28 potential of hydrazine oxidation (-0.65 V) to the inflection point (0.25 V). As the potential rises  
29 above 0.25 V, this current difference decreases with increasing potentials. In principle, this differ-  
30 ence should fall down to zero for sufficiently large potentials where the oxidation of hydrazine  
31 becomes limited by diffusion instead of electron transfer.

32 To correlate the kinetic difference between Pt and GNP with the change of the current step  
33 size as a function of potential, we plot in black in

34 Figure 5B the ratio of  $\Delta i$  and the current on Pt ( $i_{Pt}$ ). The quantity  $\Delta i/i_{Pt}$  would correspond to a  
35 situation where a 5  $\mu\text{m}$  radius carbon disk completely covers our 5  $\mu\text{m}$  radius Pt UME. From -0.8  
36 V to -0.6 V the quantity  $\Delta i/i_{Pt}$  varies abruptly with a discontinuity at -0.7 V caused by a crossing of



1 the X-axis. The variations observed at these potentials are caused by extremely small variations of  
2 the baseline current and will not be discussed further. Importantly, the quantity  $\Delta i/i_{Pt}$  equals 1 up to  
3 0 V and decreases with increasing potential due to the oxidation of hydrazine on the C fiber. The  
4 potential dependence of this curve is directly correlated with the kinetics of hydrazine oxidation on  
5 the C fibre since the hydrazine oxidation current on Pt is constant in this potential range (diffusion  
6 limited). The red points in

7 Figure 5B represent the average relative step size corresponding to GNPs colliding on the Pt  
8 UME. They are associated with the right red scale chosen in a way that the average step size at 0 V  
9 and -0.3 V coincides with the value of 1 in the black curve, and that the relative range is identical  
10 to the left black scale. This choice of scale allows a comparison of the differences in kinetics inde-  
11 pendently of the difference in size between the UME and the GNPs. The red line is a logistic func-  
12 tion adjusted on our experimental point in order to guide the eyes. The trend evidenced by collision  
13 (red points) is similar to the trend observed by cyclic voltammetry, that is first a plateau and then a  
14 decrease of the relative kinetic difference for large overpotentials. This trend is directly related to  
15 the kinetics of hydrazine oxidation on GNP since the current on Pt is constant in this potential  
16 range. Since the data points correspond to the average amplitude of the collision current step, the  
17 measured kinetics is an averaged value over the GNP size distribution and collision position on the  
18 Pt UME. The shift ( $\sim 70$  mV) between the red points ( $\Delta i/i_{ini}$  for GNP collision) and the black curve  
19 indicates slower kinetics of hydrazine oxidation on GNP than on C fiber. This observation is in  
20 agreement with a separate set of experiments evidencing kinetic blocking of hydrazine oxidation  
21 by GNP colliding on C-fiber UMEs (see Figure S2 in SI).

22 As mentioned above, the estimated hydrazine oxidation kinetics on GNP is an average value.  
23 Obtaining such information on single GNP requires (i) to determine the size and the position on the  
24 Pt UME of the GNP, and (ii) to perform numerical simulations of the GNP with its size and position  
25 to determine the expected collision current step. This is out of the scope of this work.

#### 26 4. Conclusion

27 We report a strategy, electro-catalytic depression, based on the intrinsic difference in electron  
28 transfer kinetics between materials to detect poorly catalytic particles such as GNPs. We show that  
29 our approach leads to the detection of individual GNPs of a few  $\mu\text{m}$  in length suspended at the  
30 concentration of 35 fM. More than 90% of the collisions lead to the irreversible adsorption of the  
31 GNP on the Pt surface. The current steps can be analyzed based on models already developed for  
32 insulating particles and the variation of their magnitude as a function of the potential can be ration-  
33 alized with respect to the intrinsic difference in kinetics between the electrode and GNPs. We also  
34 show that despite measuring well-defined current signals (staircase-shape, low noise), a large dis-  
35 persion of size and shape of the GNP, the poor stability of the GNP suspension, interactions be-  
36 tween GNPs adsorbed on the electrode and the edge effect should be carefully considered before  
37 attempting any quantitative analysis of the data. The ECD method is expected to be applicable to a  
38 large variety of particles thanks to the diversity of electrocatalytic reactions.

#### 39 Associated Content

40 **Supporting Information.** The following elements can be found in Supporting Information: effect  
41 of pH on the oxidation of hydrazine, the kinetics of hydrazine oxidation on GNP versus C-fiber,  
42

1 characterization of the GNP size by SEM, the shape of the current events, numerical simulations  
2 about a disk-shaped GNP blocking at a Pt UME, sedimentation of large GNPs, collision frequency  
3 vs. concentration of GNP and step size vs. potential.

4

#### 5 **Author Contributions**

6 The manuscript was written through the contributions of all authors. All authors have given ap-  
7 proval to the final version of the manuscript.

#### 8 **Acknowledgment**

9 This work is support by the CNRS, the Agence Nationale de la Recherche (ANR-17-CE09-0034-  
10 01, “SEE”) and the China Scholarship Council (201706370055). J.E.D. acknowledges The Univer-  
11 sity of North Carolina at Chapel Hill for Start-Up funds supporting this work

## 1 REFERENCES

- 2
- 3
- 4
- 5 [1] X. Xiao, A.J. Bard, Observing Single Nanoparticle Collisions at an Ultramicroelectrode  
6 by Electrocatalytic Amplification, *J. Am. Chem. Soc.*, 129 (2007) 9610-9612.
- 7 [2] X. Xiao, F.-R.F. Fan, J. Zhou, A.J. Bard, Current transients in single nanoparticle  
8 collision events, *Journal of the American Chemical Society*, 130 (2008) 16669-16677.
- 9 [3] B.-K. Kim, A. Boika, J. Kim, J.E. Dick, A.J. Bard, Characterizing Emulsions by  
10 Observation of Single Droplet Collisions · Attoliter Electrochemical Reactors, *Journal of*  
11 *the American Chemical Society*, 136 (2014) 4849-4852.
- 12 [4] J.E. Dick, C. Renault, B.K. Kim, A.J. Bard, Simultaneous detection of single attoliter  
13 droplet collisions by electrochemical and electrogenerated chemiluminescent responses,  
14 *Angew. Chem. Int. Ed.*, 53 (2014) 11859-11862.
- 15 [5] X.-W. Zhang, A. Hatami, A.G. Ewing, Simultaneous Quantification of Vesicle Size  
16 and Catecholamine Content by Resistive Pulses in Nanopores and Vesicle Impact  
17 Electrochemical Cytometry, *Journal of the American Chemical Society*, 142 (2020) 4093-  
18 4097.
- 19 [6] E. Lebègue, C.M. Anderson, J.E. Dick, L.J. Webb, A.J. Bard, Electrochemical detection  
20 of single phospholipid vesicle collisions at a Pt ultramicroelectrode, *Langmuir*, 31 (2015)  
21 11734-11739.
- 22 [7] H. Toh, R. Compton, Electrochemical detection of single micelles through ‘nano-  
23 impacts’, *Chemical science*, 6 (2015) 5053-5058.
- 24 [8] J.E. Dick, C. Renault, A.J. Bard, Observation of single-protein and DNA  
25 macromolecule collisions on ultramicroelectrodes, *Journal of the American Chemical*  
26 *Society*, 137 (2015) 8376-8379.
- 27 [9] J.Y. Lee, B.-K. Kim, M. Kang, J.H. Park, Label-free detection of single living bacteria  
28 via electrochemical collision event, *Scientific reports*, 6 (2016) 30022.
- 29 [10] E. Laborda, A. Molina, C. Batchelor - McAuley, R.G. Compton, Individual Detection  
30 and Characterization of Non - Electrocatalytic, Redox - Inactive Particles in Solution by  
31 using Electrochemistry, *ChemElectroChem*, 5 (2018) 410-417.
- 32 [11] B.M. Quinn, P.G. van't Hof, S.G. Lemay, Time-resolved electrochemical detection of  
33 discrete adsorption events, *Journal of the American Chemical Society*, 126 (2004) 8360-  
34 8361.
- 35 [12] S.E. Fosdick, M.J. Anderson, E.G. Nettleton, R.M. Crooks, Correlated  
36 electrochemical and optical tracking of discrete collision events, *Journal of the American*  
37 *Chemical Society*, 135 (2013) 5994-5997.
- 38 [13] Z. Deng, R. Elattar, F. Maroun, C. Renault, In Situ Measurement of the Size  
39 Distribution and Concentration of Insulating Particles by Electrochemical Collision on  
40 Hemispherical Ultramicroelectrodes, *Anal. Chem.*, 90 (2018) 12923-12929.
- 41 [14] A. Boika, A.J. Bard, Time of First Arrival in Electrochemical Collision Experiments  
42 as a Measure of Ultralow Concentrations of Analytes in Solution, *Anal. Chem.*, 87 (2015)  
43 4341-4346.
- 44 [15] P.A. Defnet, C. Han, B. Zhang, Temporally-Resolved Ultrafast Hydrogen Adsorption  
45 and Evolution on Single Platinum Nanoparticles, *Anal. Chem.*, 91 (2019) 4023-4030.

- 1 [16] K.J. Stevenson, K. Tschulik, A materials driven approach for understanding single  
2 entity nano impact electrochemistry, *Current Opinion in Electrochemistry*, 6 (2017) 38-45.
- 3 [17] S.E. Kleijn, S.C. Lai, T.S. Miller, A.I. Yanson, M.T. Koper, P.R. Unwin, Landing and  
4 catalytic characterization of individual nanoparticles on electrode surfaces, *Journal of the*  
5 *American Chemical Society*, 134 (2012) 18558-18561.
- 6 [18] S.E. Kleijn, B. Serrano-Bou, A.I. Yanson, M.T. Koper, Influence of hydrazine-  
7 induced aggregation on the electrochemical detection of platinum nanoparticles, *Langmuir*,  
8 29 (2013) 2054-2064.
- 9 [19] Z.p. Xiang, H.q. Deng, P. Peljo, Z.y. Fu, S.l. Wang, D. Mandler, G.q. Sun, Z.x. Liang,  
10 Electrochemical dynamics of a single platinum nanoparticle collision event for the  
11 hydrogen evolution reaction, *Angew. Chem. Int. Ed.*, 130 (2018) 3522-3526.
- 12 [20] S.J. Kwon, H. Zhou, F.-R.F. Fan, V. Vorobyev, B. Zhang, A.J. Bard, Stochastic  
13 electrochemistry with electrocatalytic nanoparticles at inert ultramicroelectrodes—theory  
14 and experiments, *Physical Chemistry Chemical Physics*, 13 (2011) 5394-5402.
- 15 [21] B.-K. Kim, J. Kim, A.J. Bard, Electrochemistry of a Single Attoliter Emulsion Droplet  
16 in Collisions, *J. Am. Chem. Soc.*, 137 (2015) 2343-2349.
- 17 [22] Y.G. Zhou, N.V. Rees, R.G. Compton, The electrochemical detection and  
18 characterization of silver nanoparticles in aqueous solution, *Angew. Chem. Int. Ed.*, 50  
19 (2011) 4219-4221.
- 20 [23] M.V. Evers, M. Bernal, B. Roldan Cuenya, K. Tschulik, Piece by Piece—  
21 Electrochemical Synthesis of Individual Nanoparticles and their Performance in ORR  
22 Electrocatalysis, *Angew. Chem. Int. Ed.*, 58 (2019) 8221-8225.
- 23 [24] K. Ngamchuea, R.O. Clark, S.V. Sokolov, N.P. Young, C. Batchelor - McAuley, R.G.  
24 Compton, Single Oxidative Collision Events of Silver Nanoparticles: Understanding the  
25 Rate - Determining Chemistry, *Chemistry - A European Journal*, 23 (2017) 16085-16096.
- 26 [25] W. Ma, H. Ma, J.-F. Chen, Y.-Y. Peng, Z.-Y. Yang, H.-F. Wang, Y.-L. Ying, H. Tian,  
27 Y.-T. Long, Tracking motion trajectories of individual nanoparticles using time-resolved  
28 current traces, *Chemical science*, 8 (2017) 1854-1861.
- 29 [26] S.M. Oja, D.A. Robinson, N.J. Vitti, M.A. Edwards, Y. Liu, H.S. White, B. Zhang,  
30 Observation of multipeak collision behavior during the electro-oxidation of single Ag  
31 nanoparticles, *Journal of the American Chemical Society*, 139 (2017) 708-718.
- 32 [27] J. Ustarroz, M. Kang, E. Bullions, P.R. Unwin, Impact and oxidation of single silver  
33 nanoparticles at electrode surfaces: one shot versus multiple events, *Chemical science*, 8  
34 (2017) 1841-1853.
- 35 [28] J.H. Park, S.N. Thorgaard, B. Zhang, A.J. Bard, Single particle detection by area  
36 amplification: single wall carbon nanotube attachment to a nanoelectrode, *Journal of the*  
37 *American Chemical Society*, 135 (2013) 5258-5261.
- 38 [29] B. Zhang, L. Fan, H. Zhong, Y. Liu, S. Chen, Graphene Nanoelectrodes: Fabrication  
39 and Size-Dependent Electrochemistry, *J. Am. Chem. Soc.*, 135 (2013) 10073-10080.
- 40 [30] J. Poon, C. Batchelor-McAuley, K. Tschulik, R.G. Compton, Single graphene  
41 nanoplatelets: capacitance, potential of zero charge and diffusion coefficient, *Chemical*  
42 *Science*, 6 (2015) 2869-2876.
- 43 [31] L. Kavan, J.H. Yum, M. Grätzel, Optically transparent cathode for dye-sensitized solar  
44 cells based on graphene nanoplatelets, *Acs Nano*, 5 (2011) 165-172.

- 1 [32] L. Kavan, J.-H. Yum, M. Grätzel, Graphene nanoplatelets outperforming platinum as  
2 the electrocatalyst in co-bipyridine-mediated dye-sensitized solar cells, *Nano Lett.*, 11  
3 (2011) 5501-5506.
- 4 [33] R.I. Jafri, N. Rajalakshmi, S. Ramaprabhu, Nitrogen doped graphene nanoplatelets as  
5 catalyst support for oxygen reduction reaction in proton exchange membrane fuel cell, *J.*  
6 *Mater. Chem.*, 20 (2010) 7114-7117.
- 7 [34] Y. Shao, S. Zhang, C. Wang, Z. Nie, J. Liu, Y. Wang, Y. Lin, Highly durable graphene  
8 nanoplatelets supported Pt nanocatalysts for oxygen reduction, *J. Power Sources*, 195  
9 (2010) 4600-4605.
- 10 [35] J. Han, L.L. Zhang, S. Lee, J. Oh, K.-S. Lee, J.R. Potts, J. Ji, X. Zhao, R.S. Ruoff, S.  
11 Park, Generation of B-doped graphene nanoplatelets using a solution process and their  
12 supercapacitor applications, *ACS nano*, 7 (2013) 19-26.
- 13 [36] B. Zhang, Q. Li, T. Cui, Ultra-sensitive suspended graphene nanocomposite cancer  
14 sensors with strong suppression of electrical noise, *Biosens. Bioelectron.*, 31 (2012) 105-  
15 109.
- 16 [37] S. Golabi, H.R. Zare, Electrocatalytic oxidation of hydrazine at glassy carbon  
17 electrode modified with electrodeposited film derived from caffeic acid, *Electroanalysis: An International Journal Devoted to Fundamental and Practical Aspects of Electroanalysis*,  
18 11 (1999) 1293-1300.
- 19 [38] L.R. Faulkner, A.J. Bard, *Electrochemical methods: fundamentals and applications*,  
20 2nd Edition, John Wiley and Sons 2002.
- 21 [39] C.-H. Chen, L. Jacobse, K. McKelvey, S.C. Lai, M.T. Koper, P.R. Unwin,  
22 Voltammetric scanning electrochemical cell microscopy: dynamic imaging of hydrazine  
23 electro-oxidation on platinum electrodes, *Anal. Chem.*, 87 (2015) 5782-5789.
- 24 [40] P.V. Dudin, P.R. Unwin, J.V. Macpherson, Electro-oxidation of hydrazine at gold  
25 nanoparticle functionalised single walled carbon nanotube network ultramicroelectrodes,  
26 *Physical Chemistry Chemical Physics*, 13 (2011) 17146-17152.
- 27 [41] L. Aldous, R.G. Compton, The mechanism of hydrazine electro-oxidation revealed by  
28 platinum microelectrodes: role of residual oxides, *Physical Chemistry Chemical Physics*,  
29 13 (2011) 5279-5287.
- 30 [42] G. Yue, Q. Zeng, J. Huang, L. Wang, Mechanism studies of hydrazine electro-  
31 oxidation by a platinum ultramicroelectrode: Effects of supporting electrolytes, *J.*  
32 *Electroanal. Chem.*, 818 (2018) 19-25.
- 33 [43] A.C. Arulrajan, C. Renault, S.C. Lai, How changes in interfacial pH lead to new  
34 voltammetric features: the case of the electrochemical oxidation of hydrazine, *Physical*  
35 *Chemistry Chemical Physics*, 20 (2018) 11787-11793.
- 36 [44] S. Kashyap, S. Mishra, S.K. Behera, Aqueous colloidal stability of graphene oxide  
37 and chemically converted graphene, *Journal of Nanoparticles*, 2014 (2014).
- 38 [45] C.-H. Chen, E.R. Ravenhill, D. Momotenko, Y.-R. Kim, S.C. Lai, P.R. Unwin, Impact  
39 of surface chemistry on nanoparticle-electrode interactions in the electrochemical  
40 detection of nanoparticle collisions, *Langmuir*, 31 (2015) 11932-11942.
- 41 [46] R. Dasari, K. Tai, D.A. Robinson, K.J. Stevenson, Electrochemical monitoring of  
42 single nanoparticle collisions at mercury-modified platinum ultramicroelectrodes, *ACS*  
43 *nano*, 8 (2014) 4539-4546.
- 44

1 [47] D.A. Robinson, A.M. Kondajji, A.D. Castañeda, R. Dasari, R.M. Crooks, K.J.  
2 Stevenson, Addressing colloidal stability for unambiguous electroanalysis of single  
3 nanoparticle impacts, *The journal of physical chemistry letters*, 7 (2016) 2512-2517.

4

5

## 1 **Figure captions**

2  
3 **Figure 1.** (A) Cyclic voltammograms recorded on a 5  $\mu\text{m}$  radius Pt UME (red traces) and a 3.5  
4  $\mu\text{m}$  radius C-fiber UME (black traces). The continuous and dashed lines correspond to cyclic  
5 voltammograms recorded in the absence and the presence of 1 mM hydrazine, respectively.  
6  $[\text{NaOH}] = 10 \mu\text{M}$ , scan rate = 20 mV/s. (B) The size distribution of GNPs is obtained by SEM.  
7 The inset is a typical SEM picture of GNPs adsorbed on glassy carbon. Because GNPs do not  
8 have a well-defined geometry, the “size” of each GNP is estimated by averaging the longest  
9 and shortest axes. Total number of GNP = 702, bin size = 1  $\mu\text{m}$ . The black line is the best fit of  
10 a Gaussian function. The center, standard deviation, and  $R^2$  are 4.2  $\mu\text{m}$ , 2.5  $\mu\text{m}$ , and 0.98, re-  
11 spectively.

12  
13 **Figure 2.** (A) Chronoamperograms recorded in the absence (black trace) and the presence (red  
14 trace) of 35 fM GNPs on a 5  $\mu\text{m}$  radius Pt UME. The UME is biased at 0 V and the solution  
15 contains 1 mM hydrazine and 10  $\mu\text{M}$  NaOH. (B) Zoom on typical current events recorded in  
16 the same condition as (A). (C) Scheme illustrating the collision of GNP on Pt UME.

17  
18 **Figure 3.** Average frequency of collision (the error bars represent the standard deviation of  
19 eleven individual experiments) as a function of the concentration of GNP. Only the first six  
20 collisions are counted on each chronoamperogram. The 5  $\mu\text{m}$  radius Pt UME is biased at 0 V  
21 and the solution contains 1 mM of hydrazine and 10  $\mu\text{M}$  of NaOH.

22  
23 **Figure 4.** Plots showing the normalized size distribution of the relative current steps caused by  
24 GNPs colliding on a 5  $\mu\text{m}$  radius Pt UME under different potentials at an orange curve: 1.0 V,  
25 210 counts, blue curve: 0.7 V, 202 counts, red curve: 0 V, 198 counts, black curve: -0.3 V, 201  
26 counts, respectively. Bin size = 3.5, the points show the center of each bin and the maximum  
27 range is limited to 24.5% in order to better compare the data, accounting the majority of the  
28 data (over 96% of total counts). In each chronoamperogram, only the first 6 GNPs colliding on  
29 a bare UME are counted to avoid the effect of GNP stacking.  $[\text{GNP}] = 35 \text{ fM}$  in 1 mM hydrazine  
30 and 10  $\mu\text{M}$  NaOH.

31  
32 **Figure 5.** (A) Difference between the adimensional linear voltammograms of Pt and C-fiber.  
33 Data is taken from Figure 1A, and normalized by the diffusion-limited steady-state current from  
34 Eq. 1. The black curve and the red curve correspond to the hydrazine oxidation occurring on a  
35 Pt UME and a C-fiber UME with the same radius as Pt. The Blue curve is the kinetic difference  
36 between the adimensional currents measured on Pt ( $i_{Pt}$ ) and on C-fiber ( $i_{C-fiber}$ ). (B) Left y-axis:  
37 The kinetic difference of hydrazine oxidation ( $\Delta i$ ) on Pt versus C-fiber is divided by the current  
38 on Pt ( $i_{Pt}$ ). The  $\Delta i/i_{Pt}$  varies with the potential. The cross line close to -0.6 V is due to the inter-  
39 section of non-faradaic currents on Pt and C-fiber. Right y-axis: the red points correspond to  
40 the relative current step size at different potentials given in Table 1, and the red curve is a fit of  
41 a logistic function performed only to guide the eyes.